Higher-Order Topology in Bismuth

Frank Schindler[1], **Zhijun Wang**[2], **Maia G. Vergniory**[3,4,5], **Ashley M. Cook**[1], **Anil Murani**[6], **Shamashis Sengupta**[7], **Alik Yu. Kasumov**[6,8], **Richard Deblock**[6], **Sangjun Jeon**[9], **Ilya Drozdov**[10], **Hélène Bouchiat**[6], **Sophie Guéron**[6], **Ali Yazdani**[9], **B. Andrei Bernevig**[9], and **Titus Neupert**[1]

[1]Department of Physics, University of Zurich, Winterthurerstrasse 190, 8057 Zurich, Switzerland [2]Department of Physics, Princeton University, Princeton, New Jersey 08544, USA [3]Donostia International Physics Center, P. Manuel de Lardizabal 4, 20018 Donostia-San Sebastian, Spain [4]Department of Applied Physics II, Faculty of Science and Technology, University of the Basque Country UPV/EHU, Apartado 644, 48080 Bilbao, Spain [5]IKERBASQUE, Basque Foundation for Science, Maria Diaz de Haro 3, 48013 Bilbao, Spain [6]LPS, Univ. Paris-Sud, CNRS, UMR 8502, F-91405 Orsay Cedex, France [7]CSNSM, Univ. Paris-Sud, IN2P3, UMR 8609, F-91405 Orsay Cedex, France [8]Institute of Microelectronics Technology and High Purity Materials, RAS, ac. Ossipyan, 6, Chernogolovka, Moscow Region, 142432, Russia [9]Joseph Henry Laboratories and Department of Physics, Princeton University, Princeton, New Jersey 08544, USA [10]Condensed Matter Physics and Materials Science Department, Brookhaven National Laboratory, Upton, New York 11973, USA

Abstract

The mathematical field of topology has become a framework to describe the low-energy electronic structure of crystalline solids. A typical feature of a bulk insulating three-dimensional topological crystal are conducting two-dimensional surface states. This constitutes the topological bulk-boundary correspondence. Here, we establish that the electronic structure of bismuth, an element consistently described as bulk topologically trivial, is in fact topological and follows a generalized bulk-boundary correspondence of higher-order: not the surfaces of the crystal, but its hinges host topologically protected conducting modes. These hinge modes are protected against localization by time-reversal symmetry locally, and globally by the three-fold rotational symmetry and inversion symmetry of the bismuth crystal. We support our claim theoretically and experimentally. Our theoretical analysis is based on symmetry arguments, topological indices, first-principle calculations, and the recently introduced framework of topological quantum chemistry. We provide supporting evidence from two complementary experimental techniques. With scanning-

tunneling spectroscopy, we probe the unique signatures of the rotational symmetry of the one-dimensional states located at step edges of the crystal surface. With Josephson interferometry, we demonstrate their universal topological contribution to the electronic transport. Our work establishes bismuth as a higher-order topological insulator.

Electronic insulators are characterized by an energy gap between valence and conduction bands. Two insulators are classified as topologically equivalent, if they can be deformed into one another without closing this gap, while certain symmetries are respected. If time-reversal symmetry (TRS) is respected in this deformation process, three-dimensional (3D) insulators have been shown to fall into two disconnected topological classes: trivial and nontrivial[1–7]. The latter are called topological insulators (TIs). What makes this mathematical classification highly relevant experimentally is the so-called bulk-boundary correspondence of TIs: the two-dimensional (2D) surface of a 3D TI hosts conducting states, with the dispersion of a non-degenerate Dirac cone, which cannot be gapped or localized without breaking TRS (or inducing interacting instabilities such as superconductivity or topological order). When, in addition, the spatial symmetries of the crystal are preserved during this deformation process, such as mirrors or rotations, one speaks of topological crystalline insulators[8–13]. The additional symmetries were argued to stabilize multiple Dirac cones on surfaces that are invariant under both TRS and the protecting spatial symmetry.

More recently, topological crystalline insulators were generalized to also include *higher-order topological insulators* (HOTIs)[14,15], in which gapless topological states protected by spatial symmetries appear at corners or hinges, while the edges and surfaces are gapped in 2D and 3D systems, respectively. HOTIs thus generalize the topological bulk-boundary correspondence. While the topological protection of point-like corner modes requires some spectral symmetry, one-dimensional gapless hinge modes mediate a spectral flow[15–18] between valence and conduction band of the bulk insulator, akin to quantum Hall[19–22] or quantum spin Hall edge modes[23–30]. Therefore, they can be expected to appear more generically in actual crystalline materials. Several works studied the classification of HOTIs[16,18,31–36], for example in the presence of two-fold spatial symmetries[16] or $\hat{C}_n$ rotational symmetries[37].

Various topological aspects of the electronic structure of bismuth have been studied experimentally in the past. This revealed intriguing features such as one-dimensional topological modes localized along step edges on the surface of bismuth[38], conducting hinge channels on bismuth nanowires[39,40], quasi-one-dimensional metallic states on the bismuth (114) surface[41], and a quantum spin Hall effect in 2D bismuth bilayers[42,43] and bismuthene on silicon carbide[44]. Here, we show, based on band representations and the theory of topological quantum chemistry[45–50], that bismuth is in fact a HOTI. This finding provides a unified theoretical origin for all these previous experimental observations. The crystal symmetries that protect the topology of bismuth, $\hat{C}_3$ rotation and inversion, establish a new class of HOTIs not discussed in previous works[14–18,31–36,51]. We support our theoretical analysis with experimental data using two complementary techniques: scanning

tunneling microscopy/spectroscopy (STM/STS) on surface step edges and Josephson interferometry on bismuth nanowires.

Another 3D material that hosts one-dimensional modes on its surface is the topological crystalline insulator tin telluride. For one, strained tin telluride is proposed to become a HOTI[15]. In addition, tin telluride has been experimentally shown to feature one-dimensional flatband modes localized at surface step edges[52]. The latter appear together with the Dirac cone topological surface states and are thus distinct from the hinge modes of a HOTI.

Note that while there are analog experimental realizations of 2D second-order topological insulators via electrical circuits[53], as well as phononic[54] and photonic[55] systems, the present work provides the first instance of a realization of the concept in the electronic structure of a crystal. At the same time, it is the first experimental confirmation of a 3D HOTI, regardless of the platform.

Bulk topology

Fu and Kane[5] gave a simple topological index for a 3D TI in the presence of inversion symmetry $\hat{I}$: One multiplies the inversion eigenvalues (which are ± 1) of all Kramers pairs of occupied bands at all time-reversal symmetric momenta (TRIMs) in the Brillouin zone. If this product is -1 ($+1$), the insulator is topological (trivial). In the topological case, one says the material has a band inversion. Note that when we evaluate this index for bismuth, we obtain $+1$, in accordance with the well known result that the band structure of bismuth is topologically trivial from a first-order perspective[56]. A sample of bismuth thus does not have topologically protected gapless surface states. However, this is not due to bismuth not displaying a band inversion: in fact, we will show that there are two band inversions, the presence of which is not captured by the first-order index, which is only sensitive to the parity of band inversions. We first extend this index to HOTIs with TRS, $\hat{C}_3$ rotation, and inversion symmetry $\hat{I}$. Note that we consider a $\hat{C}_3$ rotational symmetry with axis that is given by the line connecting the TRIMs Γ and T [consult Fig. 1 a) for a representation of the Brillouin zone]. For spin-1/2 particles, $\hat{C}_3$ has eigenvalues -1 and $\exp(\pm i\pi/3)$, where a subspace with -1 eigenvalue is closed under TRS, while TRS maps the $\exp(+i\pi/3)$ subspace to the $\exp(-i\pi/3)$ one and vice versa. We can thus define a band inversion separately in the occupied band subspaces of an insulator with $\hat{C}_3$ eigenvalues -1 and $\exp(\pm i\pi/3)$. To do so, observe that of the eight TRIMs, two are invariant under $\hat{C}_3$ (Γ and T), while two groups of three TRIMS transform into each other under $\hat{C}_3$ (call them X_i and L_i, $i = 1, 2, 3$). Denote by $\nu_Y = \prod_{i \in \text{occ}} \xi_{i,Y}$ the product over all inversion eigenvalues $\xi_{i,Y} = \pm 1$ of the occupied bands Kramers pairs at the TRIM $Y \in \{\Gamma, T, X_i, L_i\}$. At Γ and T we further define $\nu_Y^{(\pi)}$ and $\nu_Y^{(\pm\pi/3)}$, where the product is restricted to the Kramers pairs with $\hat{C}_3$ eigenvalues -1 and $\exp(\pm i\pi/3)$, respectively, such that $\nu_Y = \nu_Y^{(\pi)}\nu_Y^{(\pm\pi/3)}$ for $Y = \Gamma, T$. By $\hat{C}_3$ symmetry $\nu_{X_1} = \nu_{X_2} = \nu_{X_3}$ and $\nu_{L_1} = \nu_{L_2} = \nu_{L_3}$, so that the Fu-Kane index is given by $\nu = \nu_\Gamma \nu_T \nu_{X_1} \nu_{L_1}$. Consider a Kramers pair of states at X_1 together with its two degenerate $\hat{C}_3$ partners at X_2 and X_3. Out of a linear combination of these states, one can construct one Kramers pair with $\hat{C}_3$ eigenvalue -1, and two Kramers pairs with eigenvalues $\exp(\pm i\pi/3)$. This is shown explicitly in the Supplementary Information. When taking the Kramers pair at X_1 together with its

degenerate partners at X_2 and X_3 to have negative inversion eigenvalue, these $\hat{C}_3$ symmetric linear combinations also have negative inversion eigenvalue. Thus, a band inversion at X_i as measured by the Fu-Kane formula induces a single band inversion in the −1 subspace, and two (which equals no) band inversions in the $\exp(\pm i\pi/3)$ subspace. The same holds for the L_i points. We conclude that the total band inversion in the occupied subspaces with $\hat{C}_3$ eigenvalues −1 and $\exp(\pm i\pi/3)$ are given by

$$\nu^{(\pi)} = \nu_\Gamma^{(\pi)}\nu_T^{(\pi)}\nu_{X_1}\nu_{L_1}, \qquad \nu^{(\pm\pi/3)} = \nu_\Gamma^{(\pm\pi/3)}\nu_T^{(\pm\pi/3)}, \quad (1)$$

respectively. We then distinguish three cases: (i) $\nu^{(\pi)} = \nu^{(\pm\pi/3)} = +1$ for a trivial insulator, (ii) $\nu = \nu^{(\pi)}\nu^{(\pm\pi/3)} = -1$ for a $\mathbb{Z}_2$ topological insulator, and (iii) $\nu^{(\pi)} = \nu^{(\pm\pi/3)} = -1$ for a HOTI.

Thus far, our considerations apply to all crystals with TRS, $\hat{C}_3$ and $\hat{I}$. We now evaluate the above topological index for elementary bismuth, crystallizing in space group $R\bar{3}m$, No. 166, which possesses these symmetries [see Fig. 1 b)]. Even though bismuth is not an insulator, there exists a direct band gap separating valence bands from conduction bands [see Fig. 1 e)]. This allows us to evaluate the indices $\nu^{(\pi)}$ and $\nu^{(\pm\pi/3)}$ for the valence bands. We do so with the group characters obtained from first principle calculations (see methods). The result is $\nu^{(\pi)} = \nu^{(\pm\pi/3)} = -1$, which derives from $\nu_T^{(\pi)} = \nu_T^{(\pm/3)} = -1$, i.e., there is a $\hat{C}_3$-graded double band inversion at the T point. Hence, bismuth is a HOTI according to the topological index defined above (if we neglect the fact that it has a small electron and hole pocket).

As a second approach, we employ the formalism of elementary band representations[45–50] (EBR) to demonstrate the nontrivial topology. Since there is always an energy separation between valence and conduction bands, we restrict our consideration to the three doubly-degenerate valence bands shown in red in Fig. 1 e). In particular, we checked explicitly that the set of all bands at lower energy than these is topologically trivial. At TRIMs the eigenvalues of all symmetry operators have been computed (see methods). Referring to the character tables in the Bilbao Crystallographic Server (BCS)[47], we assign to all the bands their corresponding irreducible representations. The results of the eigenvalue calculations are listed in the Supplementary Information, Sec. C. They show that the valence bands can not be decomposed into any linear combination of physical EBRs (pEBR, which are EBRs that respect TRS). It is the main result of Ref. 45, that if such a decomposition is not possible, the electronic band structure of bismuth has to be topological and without a description in terms of exponentially localized Wannier states, in contraposition to the conclusion drawn from Fu-Kane's parity criterion[5]. To understand which symmetry protects this topological phase, we are repeating the symmetry eigenvalue calculation with an artificially lowered symmetry. The representative elements of point group $\bar{3}m$ are $\hat{C}_3$ around the z axis (denoted 3 in the space group names), $\hat{I}$ (denoted by overbar), two-fold rotational symmetry about the y axis (denoted 2), and mirror symmetry with respect to the x-z-plane (denoted m). After lowering the space group $R\bar{3}m$ (166) to $R3m$ (160) or $R32$ (155), a similar EBR analysis within the symmetry-reduced space groups shows that the valence bands can be decomposed into pEBRs in this case, indicating that they are topologically trivial. Therefore, neither two-

fold rotation nor mirror symmetry protects the nontrivial topology of bismuth. In contrast, as long as $\hat{I}$ is preserved, lowering it to space group $R\bar{3}$ (148), the valence bands are still topological in the sense that they can not be decomposed into pEBRs in space group 148. We conclude that the nontrivial topology is protected by $\hat{I}$ (in combination with the three-fold rotation). Notice that the rhombohedral lattice always respects the three-fold rotational symmetry. Since we learned from topological quantum chemistry that the bulk bands have no Wannier description, we expect the presence of spectral flow in Bi, and hence protected gapless modes on its boundaries. Since we know the surfaces of bismuth to be non-topological, these gapless boundaries must be hinges. This is compatible with previous works showing that Bi (111) bilayers (possibly on a substrate) host one-dimensional edge channels.[42,43]

Note that when changing the parameters of the tight binding-model of bismuth[57] slightly, it undergoes a transition from a second-order to a first-order topological insulator[58]. However, we confirmed the higher-order character of bismuth that is suggested by the original tight-binding model parameters[57] independently by performing first-principle calculations, as well an analysis in the framework of topological quantum chemistry. In particular, we took into account all occupied bands of bismuth up to its momentum-dependent energy gap. This is important since it has been shown that bands far away from this gap still contribute significantly to measurable effects, such as the unusually large g-factor of holes[59].

Bulk-boundary correspondence

We present a direct calculation which let us conclude that a TRS system with $\nu^{(\pi)} = \nu^{(\pm\pi/3)} = -1$ has to have hinge modes for terminations of the crystal that globally respect inversion symmetry or further symmetries. We consider a crystal of hexagonal shape [see Fig. 1 c)] which preserves $\hat{C}_3$ rotational and inversion symmetry. The steps outlined here in words are explicitly demonstrated using a Dirac model in the Supplementary Information, Sec. A. We think of the insulator with $\nu^{(\pi)} = \nu^{(\pm\pi/3)} = -1$ as a superposition of two topological insulators, one in each of the independent $\hat{C}_3$ subspaces. Consider adiabatically turning off any coupling between these two subspaces, while preserving the bulk gap. The resulting system has two Dirac cones (i.e., a Dirac theory represented by 4×4 matrices) on all surfaces of the crystal. Next, we seek to gap these surface Dirac cones by weakly coupling the two $\hat{C}_3$ subspaces. We want to do so while preserving the TRS, $\hat{C}_3$, and $\hat{I}$ of the crystal. Of these, TRS is the only constraint that acts locally on a given surface. From the representation theory of the 2D Dirac equation, one finds that for a TRS that squares to -1, as required for spinful electrons, there exists a unique mass term m that gaps the two Dirac cones in a time-reversal symmetric way. It remains to study how this mass term transforms under $\hat{C}_3$ and $\hat{I}$ to determine its relative sign between different surfaces of the crystal. Relative to the kinetic part of the surface Dirac theory, $m \rightarrow -m$ under inversion and $m \rightarrow +m$ under $\hat{C}_3$ (see Sec. A of the Supplementary Information for details). As a result, the sign of the mass term alternates between adjacent lateral surfaces of the hexagonal crystal [see Fig. 1 c)]. Each change of sign in the mass term is a domain wall in the Dirac theory and binds a Kramers pair of modes propagating along it. These are the one-dimensional hinge modes of the HOTI. The sign of the mass term on the top and bottom surface is not universally determined so that both patterns of hinge modes shown in Fig. 1 c) are

compatible with the bulk topology of $\nu^{(\pi)} = \nu^{(\pm\pi/3)} = -1$ (in a real system, the particular electronic structure determines which pattern has lower energy). Apart from this ambiguity, the argument presented here solely rests on the nontrivial bulk topology and is independent of the exact form of the surface electronic structure, as long as the surface is gapped while preserving the respective symmetries. This constitutes the generalized topological bulk-boundary correspondence characteristic of a HOTI, where the existence of one-dimensional hinge modes directly follows from the 3D bulk topology. The HOTI's bulk-boundary correspondence requires that these hinge modes are locally stable under time-reversal symmetric perturbations that preserve the bulk and surface gaps. From this requirement, we can understand the $\mathbb{Z}_2$ topological character of the phase: the minimal TRS surface manipulation is the addition of a 2D TI to one surface of the hexagonal nanowire. This would permit hybridizing and gapping out of the pair of hinge modes adjacent to the surface. However, to comply with $\hat{I}$ and $\hat{C}_3$, the same 2D TI has to be added to every surface, thus leaving the Kramers pairs of modes intact at each hinge. We conclude that a single Kramers pair of modes at each hinge is stable under all symmetry-preserving surface perturbations. In fact, such a Kramers pair is locally stable under small perturbations even when the spatial symmetries are broken, e.g., by introducing disorder into the sample, as long a TRS is preserved. The only way to remove it is to annihilate it with another Kramers pair coming from another hinge, which cannot be achieved with just a small perturbation. The higher-order hinge modes of a 3D HOTI are therefore just as stable as the edge modes of a first-order TRS topological insulator in 2D. We further exemplify these results with a tight-binding model, defined in Sec. B of the Supplementary Information, whose hinge states are shown in Fig. 1 d),f),g). Note that our tight-binding model is topologically equivalent to a realistic model57 of bismuth, however it is easier to interpret in the sense that it does not have metallic bulk and surface states that would obscure the hinge modes in the electronic structure plots we present here. It also has fewer orbitals per unit cell, which makes 3D simulations of large systems feasible.

We now turn to experimental data that support our higher-order bulk-boundary correspondence in bismuth. Even though bismuth is metallic in the bulk and on the surface, only its topological hinge states are protected against scattering by weak disorder as compared to trivial surface states, for example. We expect hinge states between (i) the top surface [which is denoted (111) in the primitive unit vectors] and three of the six lateral surfaces and (ii) between adjacent lateral surfaces. The geometry of the samples was more amenable to study the hinge states of type (i), as we outline below.

STM experiment

With a STM, we studied the electronic structure of step edges on the (111) surface of bismuth. Due to the buckled honeycomb structure of the bismuth bilayer along the [111] trigonal direction, STM topographic images of the (111) plane of bismuth show bilayer steps with two different types of bisectrix edges: type A and type B [marked as red and blue lines in Fig. 2 a)]. We highlight two structures of triangular and nearly hexagonal shape [Fig. 2 a) and c)]. In particular the step edge in Fig. 2 c) can be seen as (the negative of) a one bilayer tall version of the crystals shapes shown in Fig. 1 c). We thus expect hinge states at either the type A or the type B edges due to the higher-order topology. (All A type and all B type

edges are mutually equivalent due to the $\hat{C}_3$ rotational symmetry of the bismuth (111) surface.) Indeed, we observe strongly localized edge states only at type A edges in Fig. 2 b) and d), which display the differential conductance map overlaid on top of the topographic data to illuminate the edge states at the van Hove singularity energy of the bismuth edge states. A previous experimental study38 showed a one-dimensional van Hove singularity of the edge states (E = 183 meV) and quasi-particle interference of the spin-orbit locked edge states. The same study demonstrated the absence of k to $-k$ scattering for these states. These experimental observations and model calculations strongly suggest that the edge states are living in the momentum dependent energy gap of the bismuth (111) surface states38. Every other edge of a hexagonal pit exhibits localized edge states and these edge states are discontinued at the corner where type A and type B edge meet [Fig. 2 c) and d)]. This feature remarkably reproduces the hinge modes calculated for the hexagonal nanowire as shown in Fig. 1 d).

Transport experiment

We exploited proximity-induced superconductivity to reveal ballistic hinge states along monocrystalline bismuth nanowires39,40. When these (non superconducting) nanowires are connected to superconducting contacts (implementing a superconductor/bismuth nanowire/superconductor or S/Bi/S Josephson junction), a supercurrent runs through them at low temperature. Our experiments unambiguously demonstrate that the supercurrent flows via extremely few narrow one-dimensional channels, rather than via the entire surface or bulk of the nanowire. The experimental indications are the following: i) Periodic oscillations of the critical current through the nanowires caused by a magnetic field, with a period corresponding to one magnetic flux quantum through the wire section perpendicular to the field39,40. Such oscillations indicate interference between two supercurrent-carrying paths located at the nanowire edges60 (see also the Supplementary Material), since a uniform current density in such a long narrow wire would produce instead a monotonously decaying critical current. ii) The supercurrent flowing through the nanowire persists to extremely high magnetic fields, up to several Teslas in some samples. Since the orbital dephasing due to a magnetic flux through the supercurrent-carrying channel area destroys the induced supercurrent, this indicates that the channels are extremely narrow spatially. iii) Finally, we have recently provided a direct signature of ballistic transport along those one-dimensional channels, by measuring the supercurrent-versus-phase relation (also called current phase relation, or CPR) of the S/Bi/S junction. This was done by inserting the bismuth nanowires into an asymmetric superconducting quantum interference device (SQUID) configuration40,61. Whereas tunneling or diffusive transport give rise to the usual nearly sinusoidal current phase relation of superconductor/normal metal/superconductor Josephson junctions, the sharp sawtooth-shaped current phase relation we found instead, demonstrates that transport occurs ballistically along the wire. The scattering probability p was estimated to be 0.1 along the 1 μm long bismuth wire from the harmonics content of this current phase relation (where the nth harmonic decays like $(1 - p)^{2n}/n$). This leads to a lower bound of the mean free path l_e along these edges equal to 10 μm, much longer than the value l_e = 0.1 μm determined for the surface states. This surprising result is explained by the dominant contribution of the topologically protected hinge states to the supercurrent. Indeed, the

supercurrent carried by a diffusive channel is $(L/l_e)^2 \approx 100$ times smaller than the supercurrent carried by a ballistic channel (l_e and L are the elastic mean free path and wire length, respectively). The position of the edge states can be deduced from the periodicity of the SQUID oscillations, which is inversely proportional to the area enclosing the flux. In a sample of parallelogrammatic cross-section whose geometry and orientation was precisely determined, we detected a beating of two paths enclosing different fluxes Φ and Φ' [see Fig. 3 a)].40 This demonstrated that the edge states are located along the two acute edges of the (111) facets. Those edges coincide with the expected hinge states perpendicular to the trigonal [111] axis [see Fig. 3 b)]. The contribution of each path was extracted and is shown in Fig. 3 d) and e). The supercurrents carried by the two hinges differ by a factor of four. This can be explained by a difference in the quality of the contact to these hinge states: The top hinges of the wire have been more severely etched than the bottom ones during the deposition of the superconducting electrodes [see Fig. 3 a)]. This strong etching reduces the coupling of edge states to the superconducting contacts and the supercurrent is decreased even though the ballistic nature is unaffected.

Comparing Fig. 3 d) and Fig. 1 c), we note that one of the two hinges on top of the nanowire must be of A type and the other one of B type (the same is true for the bottom two hinges). Our observation of a ballistic channel at one of these hinges at the top, and one at the bottom of the nanowire, is thus in line with the theoretical expectation from the higher-order topology of bismuth.

Summary

The bismuth-antimony alloy, $Bi_{1-x}Sb_x$, was the first material realization of a 3D TI3,5. The composition x was used to interpolate between the bismuth without band inversion and the band inverted antimony. In this work, we demonstrated theoretically that the allegedly trivial end of this interpolation, bismuth, has in fact a 3D topological band structure as well. It is a HOTI with helical hinge states. We presented two complementary pieces of experimental evidence supporting this result, using STM and Josephson-interferometry measurements. The type of hinge states discussed here may be used for lossless electronic transport due to their local protection from backscattering by TRS disorder. Further applications include spintronics, due to their spin-momentum locking, and – when proximitized with superconductivity – topological quantum computation. For the latter, a nanowire with hexagonal cross-section may provide a particularly convenient way of building a hexon – a group of six Majorana states, one at each hinge. Hexons have been proposed as building blocks for a measurement-only quantum computer62.

Methods

First-principle calculations

We employed density functional theory (DFT) as implemented in the Vienna Ab Initio Simulation Package (VASP)64–67. The exchange correlation term is described according to the Perdew-Burke-Ernzerhof (PBE) prescription together with projected augmented-wave pseudopotentials68,69 and the spin-orbit interaction included. For the self-consistent calculations we used a $12 \times 12 \times 12$ k-points mesh for the bulk band structure calculations.

The eigenvalues of the symmetry transformations were deduced from the matrix representations of the respective symmetry operation calculated using the Bloch eigenstates from VASP.

STM experiment

Bismuth crystals were cleaved at room temperature in ultra-high vacuum conditions and the cleaved samples were cooled down to a temperature of 4 K at which scanning tunneling microscopy (STM) and spectroscopy (STS) measurements were carried out. The cleaved bismuth crystal exhibits a (111) plane of the bismuth rhombohedral structure [which is the (001) plane of the bismuth hexagonal structure]. The topographic data and the differential conductance maps were. For STM measurements, a mechanically sharpened platinum-iridium tip was used, and electronic properties of the probe tip were characterized before the experiments on bismuth by checking a reference sample. Differential conductance maps [Fig. 2 b) and d)] are taken simultaneously with topographic data at the van Hove singularity energy ($V = 183$ meV) of the bismuth edge states using a lock-in amplifier with an oscillation of 3 meV and with $I = 3.5$ nA. The data shown in this manuscript is reproduced on many step edges of Bi (111) with atomically different tips. All of the islands on the Bi (111) surface show the expected step height of 4 Å for bismuth bilayers and all of the extended edges are identified as zigzag structures of either A type or B type. A type and B type edges are equivalent in the hexagonal nanowire geometry as described in the main manuscript [Fig. 1 c)], however, the existence of the Bi (111) surface under the bismuth bilayer breaks the inversion symmetry, and A as well as B type edges can be identified in STM measurements. Only A type edges show the spectroscopic feature of a sharp peak at 183 meV which is the van Hove singularity energy of the one-dimensional edge state. Quasi-particle interference (QPI) measurements reveal that this edge state is continuously dispersing down to the Fermi level and starts to merge with the surface states at the momentum where the surface gap closes[38]. This spectroscopic feature of geometric confinement only at A type edges resembles the topological hinge modes expected for the hexagonal nanowire, as discussed in the main text.

Transport experiment

The nanowires grew during slow sputtering deposition of high purity bismuth on a slightly heated silicon substrate. High resolution transmission electron microscopy (TEM) indicates high quality single crystals, of hexagonal or rhombohedral cross-sections, with clear facets. The facet widths are typically 50 to 300 nm wide. Resistance measurements show that transport in the normal state (i.e., when contacts to the nanowires are not superconducting) occurs predominately due to surface states, with an elastic mean free path of the order of 100 nm.

Supplementary Material

Refer to Web version on PubMed Central for supplementary material.

Acknowledgments

References

1. Fu LiangKane CL, Mele EJ. Topological insulators in three dimensions. Phys Rev Lett. 2007; 98:106803. [PubMed: 17358555]

2. Moore JE, Balents L. Topological invariants of time-reversal-invariant band structures. Phys Rev B. 2007; 75:121306.

3. Hsieh D, Xia Y, Wray L, Qian D, Pal A, Dil JH, Osterwalder J, Meier F, Bihlmayer G, Kane CL, Hor YS, et al. Observation of unconventional quantum spin textures in topological insulators. Science. 2009; 323:919–922. [PubMed: 19213915]

4. Roy Rahul. Topological phases and the quantum spin hall effect in three dimensions. Phys Rev B. 2009; 79:195322.

5. Fu LiangKane CL. Topological insulators with inversion symmetry. Phys Rev B. 2007; 76:045302.

6. Xia Y, Qian D, Hsieh D, Wray L, Pal A, Lin H, Bansil A, Grauer D, Hor YS, Cava RJ, Hasan MZ. Observation of a large-gap topological-insulator class with a single dirac cone on the surface. Nat Phys. 2009; 5:398–402.

7. Chen YL, Analytis JG, Chu J-H, Liu ZK, Mo S-K, Qi XL, Zhang HJ, Lu DH, Dai X, Fang Z, Zhang SC, et al. Experimental realization of a three-dimensional topological insulator, Bi_2Te_3. Science. 2009; 325:178–181. http://science.sciencemag.org/content/325/5937/178.full.pdf. [PubMed: 19520912]

8. Fu Liang. Topological crystalline insulators. Phys Rev Lett. 2011; 106:106802. [PubMed: 21469822]

9. Hsieh Timothy H, Lin HsinLiu JunweiDuan WenhuiBansil ArunFu Liang. Topological crystalline insulators in the snte material class. Nat Commun. 2012; 3:982. [PubMed: 22864575]

10. Dziawa P, Kowalski BJ, Dybko K, Buczko R, Szczerbakow A, Szot M, Ausakowska E, Balasubramanian T, Wojek BM, Berntsen MH, Tjernberg O, et al. Topological crystalline insulator states in pbsnse. Nat Mater. 2012; 11:1023–1027. [PubMed: 23023551]

11. Mong Roger SK, Essin Andrew M, Moore Joel E. Antiferromagnetic topological insulators. Phys Rev B. 2010; 81:245209.

12. Tanaka Y, Ren Zhi, Sato T, Nakayama K, Souma S, Takahashi T, Segawa Kouji, Ando Yoichi. Experimental realization of a topological crystalline insulator in snte. Nat Phys. 2012; 8:800–803.

13. Xu Su-YangLiu ChangAlidoust N, Neupane M, Qian D, Belopolski I, Denlinger JD, Wang YJ, Lin H, Wray LA, Landolt G. , et al. Observation of a topological crystalline insulator phase and topological phase transition in pb1xsnxte. Nature Communications. 2012; 3 1192 EP.

14. Benalcazar Wladimir A, Bernevig B AndreiHughes Taylor L. Quantized electric multipole insulators. Science. 2017; 357:61–66. http://science.sciencemag.org/content/357/6346/61.full.pdf. [PubMed: 28684520]

15. Schindler FrankCook Ashley M, Vergniory Maia G, Wang ZhijunParkin Stuart SP, Bernevig B AndreiNeupert Titus. Higher-order topological insulators. Science Advances. 2018; 4:eaat0346. http://advances.sciencemag.org/content/4/6/eaat0346.full.pdf. [PubMed: 29869644]

16. Song ZhidaFang ZhongFang Chen. $(d-2)$-dimensional edge states of rotation symmetry protected topological states. Phys Rev Lett. 2017; 119:246402. [PubMed: 29286745]

17. Benalcazar Wladimir A, Bernevig B AndreiHughes Taylor L. Electric multipole moments, topological multipole moment pumping, and chiral hinge states in crystalline insulators. Phys Rev B. 2017; 96:245115.

18. Langbehn JosiasPeng YangTrifunovic Lukavon Oppen FelixBrouwer Piet W. Reflection-symmetric second-order topological insulators and superconductors. Phys Rev Lett. 2017; 119:246401. [PubMed: 29286744]

19. Klitzing KvDorda G, Pepper M. New method for highaccuracy determination of the fine-structure constant based on quantized hall resistance. Phys Rev Lett. 1980; 45:494–497.

20. Thouless DJ, Kohmoto M, Nightingale MP, Nijs M den. Quantized hall conductance in a two-dimensional periodic potential. Phys Rev Lett. 1982; 49:405–408.

21. Avron Joseph E, Seiler Ruedi. Quantization of the hall conductance for general, multiparticle schrödinger hamiltonians. Phys Rev Lett. 1985; 54:259–262.

22. Niu QianThouless DJ, Yong-Shi Wu. Quantized hall conductance as a topological invariant. Phys Rev B. 1985; 31:3372–3377.

23. Kane CL, Mele EJ. z_2 topological order and the quantum spin hall effect. Phys Rev Lett. 2005; 95:146802. [PubMed: 16241681]

24. Kane CL, Mele EJ. Quantum spin hall effect in graphene. Phys Rev Lett. 2005; 95:226801. [PubMed: 16384250]

25. Qi Xiao-LiangWu Yong-ShiZhang Shou-Cheng. Topological quantization of the spin hall effect in two-dimensional paramagnetic semiconductors. Phys Rev B. 2006; 74:085308.

26. Bernevig B AndreiHughes Taylor L, Zhang Shou-Cheng. Quantum spin hall effect and topological phase transition in hgte quantum wells. Science. 2006; 314:1757–1761. http://science.sciencemag.org/content/314/5806/1757.full.pdf. [PubMed: 17170299]

27. Bernevig B AndreiZhang Shou-Cheng. Quantum spin hall effect. Phys Rev Lett. 2006; 96:106802. [PubMed: 16605772]

28. König MarkusWiedmann SteffenBrüne ChristophRoth AndreasBuhmann HartmutMolenkamp Laurens W, Qi Xiao-LiangZhang Shou-Cheng. Quantum spin hall insulator state in hgte quantum wells. Science. 2007; 318:766–770. [PubMed: 17885096]

29. Roth AndreasBrüne ChristophBuhmann HartmutMolenkamp Laurens W, Maciejko JosephQi Xiao-LiangZhang Shou-Cheng. Nonlocal transport in the quantum spin hall state. Science. 2009; 325:294–297. http://science.sciencemag.org/content/325/5938/294.full.pdf. [PubMed: 19608911]

30. Wu CongjunBernevig B AndreiZhang Shou-Cheng. Helical liquid and the edge of quantum spin hall systems. Phys Rev Lett. 2006; 96:106401. [PubMed: 16605768]

31. Xu Y, Xue R, Wan S. Topological Corner States on Kagome Lattice Based Chiral Higher-Order Topological Insulator. arXiv:1711.09202 [cond-mat.str-el]. 2017 ArXiv e-prints.

32. Shapourian HassanWang YuxuanRyu Shinsei. Topological crystalline superconductivity and second-order topological superconductivity in nodal-loop materials. Phys Rev B. 2018; 97:094508.

33. Lin M, Hughes TL. Topological Quadrupolar Semimetals. arXiv:1708.08457 [cond-mat.mes-hall]. 2017 ArXiv e-prints.

34. Ezawa Motohiko. Higher-order topological insulators and semimetals on the breathing kagome and pyrochlore lattices. Phys Rev Lett. 2018; 120:026801. [PubMed: 29376716]

35. Khalaf Eslam. Higher-order topological insulators and superconductors protected by inversion symmetry. Physical Review B. 2018; 97:205136.

36. Geier MaxTrifunovic LukaHoskam MaxBrouwer Piet W. Second-order topological insulators and superconductors with an order-two crystalline symmetry. Phys Rev B. 2018; 97:205135.

37. Fang C, Fu L. Rotation Anomaly and Topological Crystalline Insulators. arXiv:1709.01929 [cond-mat.mes-hall]. 2017 ArXiv e-prints.

38. Drozdov Ilya K, Alexandradinata A, Jeon SangjunNadj-Perge StevanJi HuiwenCava RJ, Bernevig B AndreiYazdani Ali. One-dimensional topological edge states of bismuth bilayers. Nat Phys. 2014; 10:664–669.

39. Li ChuanKasumov A, Murani AnilSengupta ShamashisFortuna F, Napolskii K, Koshkodaev D, Tsirlina G, Kasumov Y, Khodos I, Deblock R. , et al. Magnetic field resistant quantum interferences in josephson junctions based on bismuth nanowires. Phys Rev B. 2014; 90:245427.

40. Murani AnilKasumov AlikSengupta ShamashisKasumov Yu A, Volkov VT, Khodos II, Brisset F, Delagrange RaphaëlleChepelianskii AlexeiDeblock RichardBouchiat Hélène, et al. Ballistic edge states in bismuth nanowires revealed by squid interferometry. Nature Communications. 2017; 8 15941.

41. Wells JW, Dil JH, Meier F, Lobo-Checa J, Petrov VN, Osterwalder J, Ugeda MM, Fernandez-Torrente I, Pascual JI, Rienks EDL, Jensen MF, et al. Nondegenerate metallic states on Bi(114)A one-dimensional topological metal. Phys Rev Lett. 2009; 102:096802. [PubMed: 19392548]

42. Murakami Shuichi. Quantum spin hall effect and enhanced magnetic response by spin-orbit coupling. Phys Rev Lett. 2006; 97:236805. [PubMed: 17280226]

43. Takayama A, Sato T, Souma S, Oguchi T, Takahashi T. One-dimensional edge states with giant spin splitting in a bismuth thin film. Phys Rev Lett. 2015; 114:066402. [PubMed: 25723232]

44. Reis F, Li G, Dudy L, Bauernfeind M, Glass S, Hanke W, Thomale R, Schäfer J, Claessen R. Bismuthene on a SiC substrate: A candidate for a high-temperature quantum spin hall material. Science. 2017; 357:287–290. [PubMed: 28663438]

45. Bradlyn BarryElcoro L, Cano JenniferVergniory MG, Wang ZhijunFelser C, Aroyo MI, Bernevig B Andrei. Topological quantum chemistry. Nature. 2017; 547:298–305. [PubMed: 28726818]

46. Vergniory MG, Elcoro L, Wang Zhijun, Cano Jennifer, Felser C, Aroyo MI, Bernevig B Andrei, Bradlyn Barry. Graph theory data for topological quantum chemistry. Phys Rev E. 2017; 96:023310. [PubMed: 28950561]

47. Elcoro LuisBradlyn BarryWang ZhijunVergniory Maia G, Cano JenniferFelser ClaudiaBernevig B AndreiOrobengoa DanelFlor G, Aroyo Mois I. Double crystallographic groups and their representations on the bilbao crystallographic server. Journal of Applied Crystallography. 2017; 50:1457–1477.

48. Cano JenniferBradlyn BarryWang ZhijunElcoro L, Vergniory MG, Felser C, Aroyo MI, Bernevig B Andrei. Building blocks of topological quantum chemistry: Elementary band representations. Phys Rev B. 2018; 97:035139.

49. Bradlyn BarryElcoro L, Vergniory MG, Cano JenniferWang ZhijunFelser C, Aroyo MI, Bernevig B Andrei. Band connectivity for topological quantum chemistry: Band structures as a graph theory problem. Phys Rev B. 2018; 97:035138.

50. Cano J, Bradlyn B, Wang Z, Elcoro L, Vergniory MG, Felser C, Aroyo MI, Bernevig BA. Topology of Disconnected Elementary Band Representations. arXiv: 1711.11045 [cond-mat.mes-hall]. 2017 ArXiv e-prints.

51. Ezawa M. Minimal model for higher-order topological insulators and phosphorene. arXiv: 1801.00437 [cond-mat.mes-hall]. 2018 ArXiv e-prints.

52. Sessi PaoloDi Sante DomenicoSzczerbakow AndrzejGlott FlorianWilfert StefanSchmidt HenrikBathon ThomasDziawa PiotrGreiter MartinNeupert TitusSangiovanni Giorgio, et al. Robust spin-polarized midgap states at step edges of topological crystalline insulators. Science. 2016; 354:1269–1273. http://science.sciencemag.org/content/354/6317/1269.full.pdf. [PubMed: 27940869]

53. Imhof S, Berger C, Bayer F, Brehm J, Molenkamp L, Kiessling T, Schindler F, Lee CH, Greiter M, Neupert T, Thomale R. Topolectrical circuit realization of topological corner modes. arXiv: 1708.03647 [condmat.mes-hall]. 2017 ArXiv e-prints.

54. Serra-Garcia MarcPeri ValerioSüsstrunk RomanBilal Osama R, Larsen TomVillanueva Luis GuillermoHuber Sebastian D. Observation of a phononic quadrupole topological insulator. Nature. 2018; 555:342–345. [PubMed: 29334685]

55. Peterson Christopher W, Benalcazar Wladimir A, Hughes Taylor L, Bahl Gaurav. A quantized microwave quadrupole insulator with topologically protected corner states. Nature. 2018; 555:346–350. [PubMed: 29542690]

56. Teo Jeffrey CY, Liang FuKane CL. Surface states and topological invariants in three-dimensional topological insulators: Application to $bi_{1-x}sb_x$. Phys Rev B. 2008; 78:045426.

57. Liu YiAllen Roland E. Electronic structure of the semimetals bi and sb. Phys Rev B. 1995; 52:1566–1577.

58. Ohtsubo YoshiyukiKimura Shin ichi. Topological phase transition of single-crystal bi based on empirical tight-binding calculations. New Journal of Physics. 2016; 18:123015.

59. Fuseya YukiZhu ZengweiFauqué BenoîtKang WounLenoir BertrandBehnia Kamran. Origin of the large anisotropic g factor of holes in bismuth. Phys Rev Lett. 2015; 115:216401. [PubMed: 26636860]

60. Hart SeanRen HechenWagner TimoLeubner PhilippMühlbauer MathiasBrüne ChristophBuhmann HartmutMolenkamp Laurens W, Yacoby Amir. Induced superconductivity in the quantum spin hall edge. Nature Physics. 2014; 10:638–643.

61. Della Rocca ML, Chauvin M, Huard B, Pothier H, Esteve D, Urbina C. Measurement of the current-phase relation of superconducting atomic contacts. Phys Rev Lett. 2007; 99:127005. [PubMed: 17930546]

62. Karzig TorstenKnapp ChristinaLutchyn Roman M, Bonderson ParsaHastings Matthew B, Nayak ChetanAlicea JasonFlensberg KarstenPlugge StephanOreg YuvalMarcus Charles M. , et al. Scalable designs for quasiparticle-poisoning-protected topological quantum computation with majorana zero modes. Phys Rev B. 2017; 95:235305.

63. Aroyo MI, Perez-Mato JM, Orobengoa D, Tasci E, De La Flor G, Kirov A. Crystallography online: Bilbao crystallographic server. Bulgarian Chemical Communications. 2011; 43:183–197.

64. Kresse G, Joubert D. From ultrasoft pseudopotentials to the projector augmented-wave method. Phys Rev B. 1999; 59:1758–1775.

65. Kresse G, Furthmueller J. Efficiency of ab-initio total energy calculations for metals and semiconductors using a plane-wave basis set. Computational Materials Science. 1996; 6:15–50.

66. Kresse G, Hafner J. *Ab initio* molecular dynamics for open-shell transition metals. Phys Rev B. 1993; 48:13115–13118.

67. Hobbs D, Kresse G, Hafner J. Fully unconstrained noncollinear magnetism within the projector augmented-wave method. Phys Rev B. 2000; 62:11556–11570.

68. Perdew John P, Burke KieronErnzerhof Matthias. Generalized gradient approximation made simple. Phys Rev Lett. 1996; 77:3865–3868. [PubMed: 10062328]

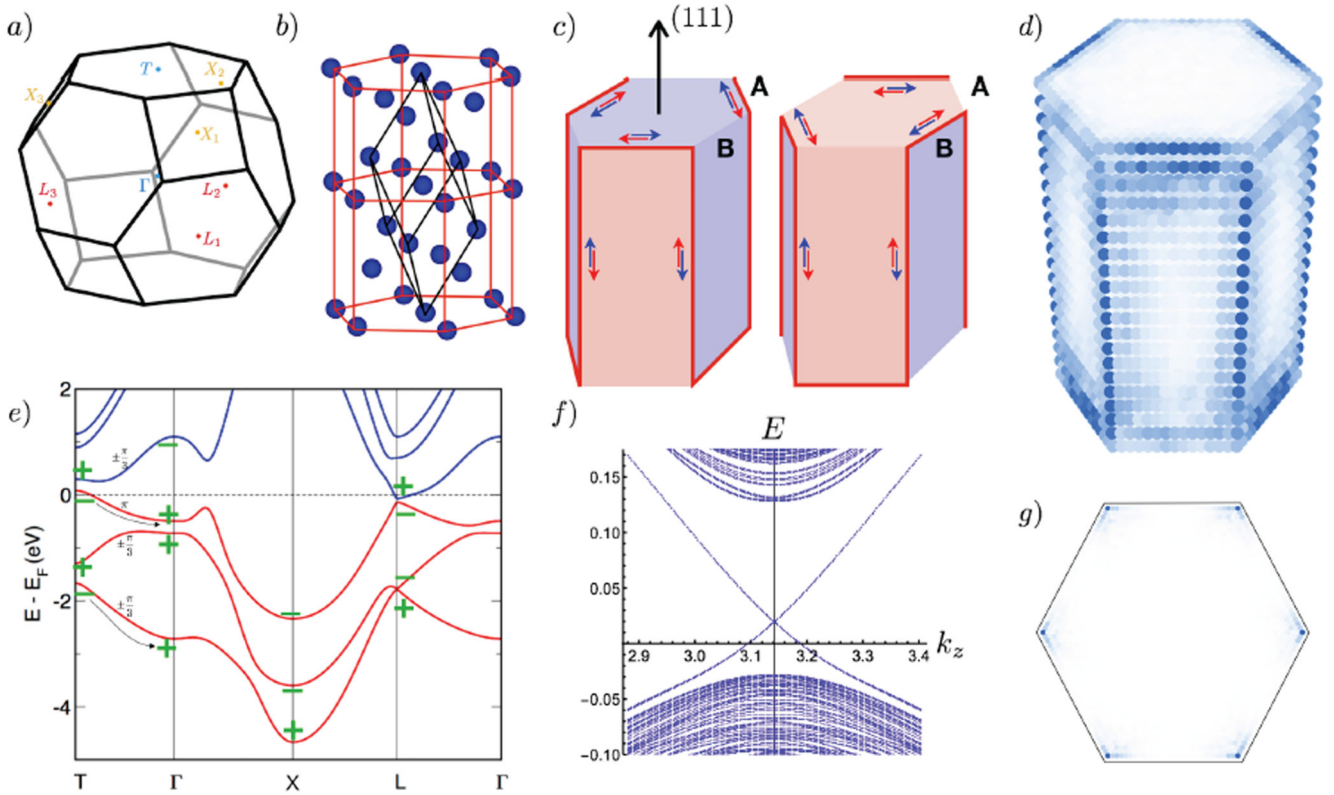69. Perdew JP, Burke K, Ernzerhof M. Perdew, burke, and ernzerhof reply: Phys Rev Lett. 1998; 80:891–891.

Fig. 1. Electronic structure of a HOTI with $\hat{C}_3$ and $\hat{I}$.
a) Brillouin zone with TRS points that are used to evaluate the topological indices in Eq. (1).
b) Unit cell of the crystal structure of bismuth, which has $\hat{C}_3$ and inversion-symmetry. There are six inequivalent sites in the conventional (hexagonal) unit cell, which is shown in red. Black lines delineate the primitive unit cell (rhombohedral), which has only 2 inequivalent atoms. c) Schematic of the hinge states of a hexagonally-shaped HOTI oriented along the trigonal [111] axis, with $\hat{C}_3$ and inversion-symmetry (e.g., bismuth). Note that a prism with triangular rather than hexagonal cross-section would would not respect inversion symmetry. All edges of the hexagonal cross-section are along bisectrix axes. Red lines represent a single one-dimensional Kramers pair of gapless protected modes. In the Dirac picture of a HOTI surface, red and blue surfaces correspond to opposite signs of the unique TRS surface mass terms. d) Localized hinge modes of the minimal tight-binding model of a HOTI with the same topology and symmetries as bismuth, as defined in the Supplementary Information. The model is solved on the hexagon geometry described in (c) with open boundary conditions in all directions. Plotted is the sum of the absolute squares of the eigenstates that lie in the bulk and surface gap. Note that while the tight-binding model considered has the same topology as bismuth, it lacks its metallic surface states which are not protected by $\hat{C}_3$ and inversion symmetry. e) Band structure of bismuth with inversion eigenvalues (green) and $\hat{C}_3$ eigenvalues on the Γ–T line (black). Since valence bands (red) and conduction bands (blue) are not degenerate anywhere in momentum space, their topological indices, Eq. (1), are well defined despite the appearance of a small electron and hole pocket. Black arrows indicate the two valence bands contributing to the $\hat{C}_3$-eigenvalue-graded band inversion. f)

Spectrum of the same model solved on a nanowire with hexagonal cross-section and periodic boundary conditions in the trigonal z direction ([111] direction). Only a portion of the spectrum at small momentum deviations from the T point $k_z = \pi$ is shown. Six Kramers pairs of hinge modes traverse the surface and bulk gap. Consult Fig. S2 c) in the Supplementary Information for a zoomed-out version showing the spectrum for all momenta. g) Localization of these topologically protected hinge modes in the x-y-plane.
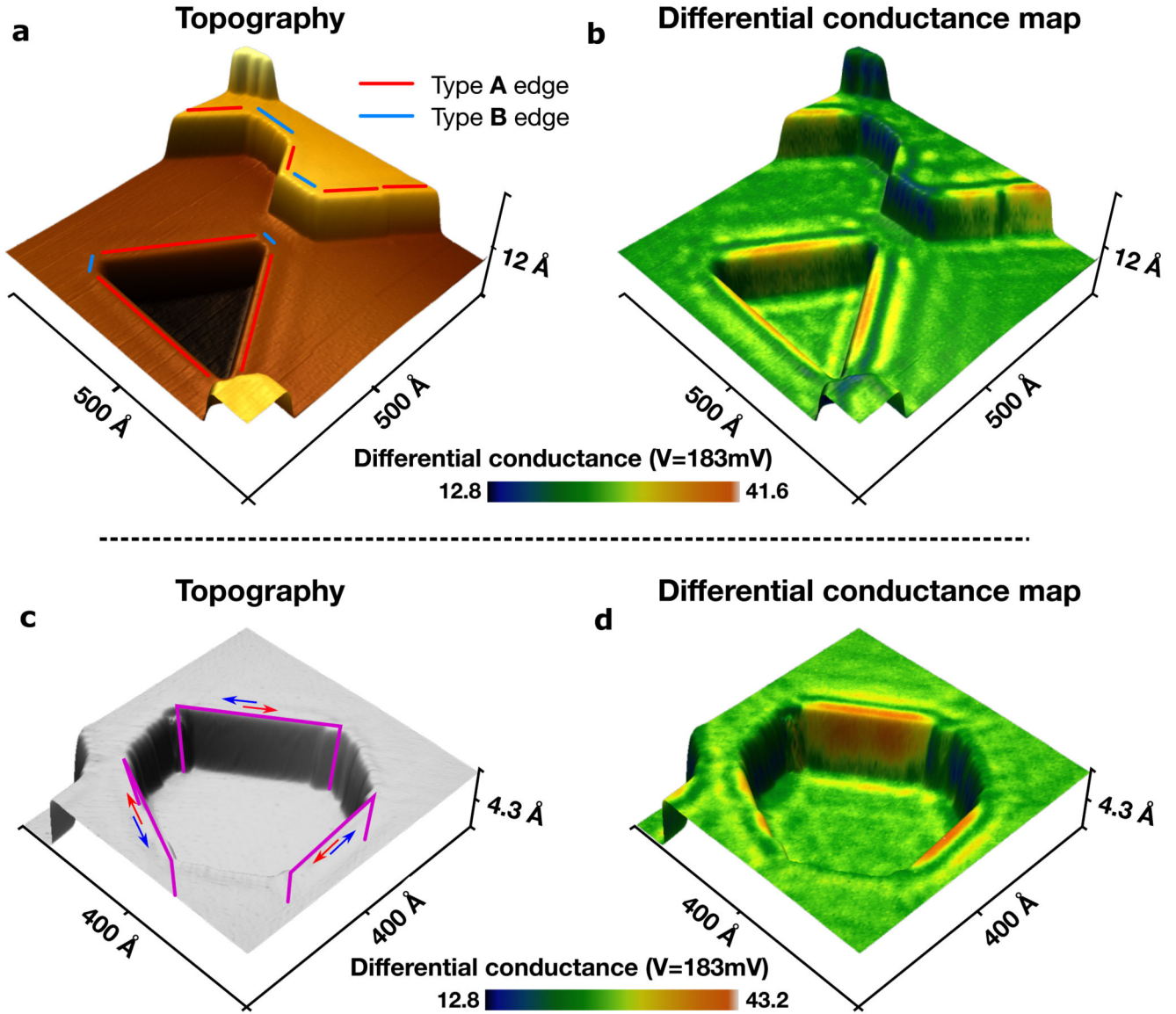
Fig. 2. Experimental observation of the alternating edge states on a bismuth (111) surface perpendicular to its trigonal axis.

a) 3D rendered topographic image of the bismuth (111) surface. The red (type A) and blue (type B) lines then indicate the types of edge, which are along bisectrix axes. Note that the edges of type B in this particular pit geometry are much shorter than edges of type A, while still large enough to be experimentally accessible. b) Differential conductance map at the van Hove singularity energy ($V = 183$ meV) of the one-dimensional edge states. In contrast to the type B edges, all the type A edges exhibit localized high conductance. c) Topographic image of a hexagonal pit on a bismuth (111) surface. The hinge modes are schematically shown as purple lines. Blue and red arrows indicate the flow of the spin-momentum locked hinge modes. d) Differential conductance map simultaneously acquired with the topographic data from c), showing high conductance at every other edge of the hexagonal pit.
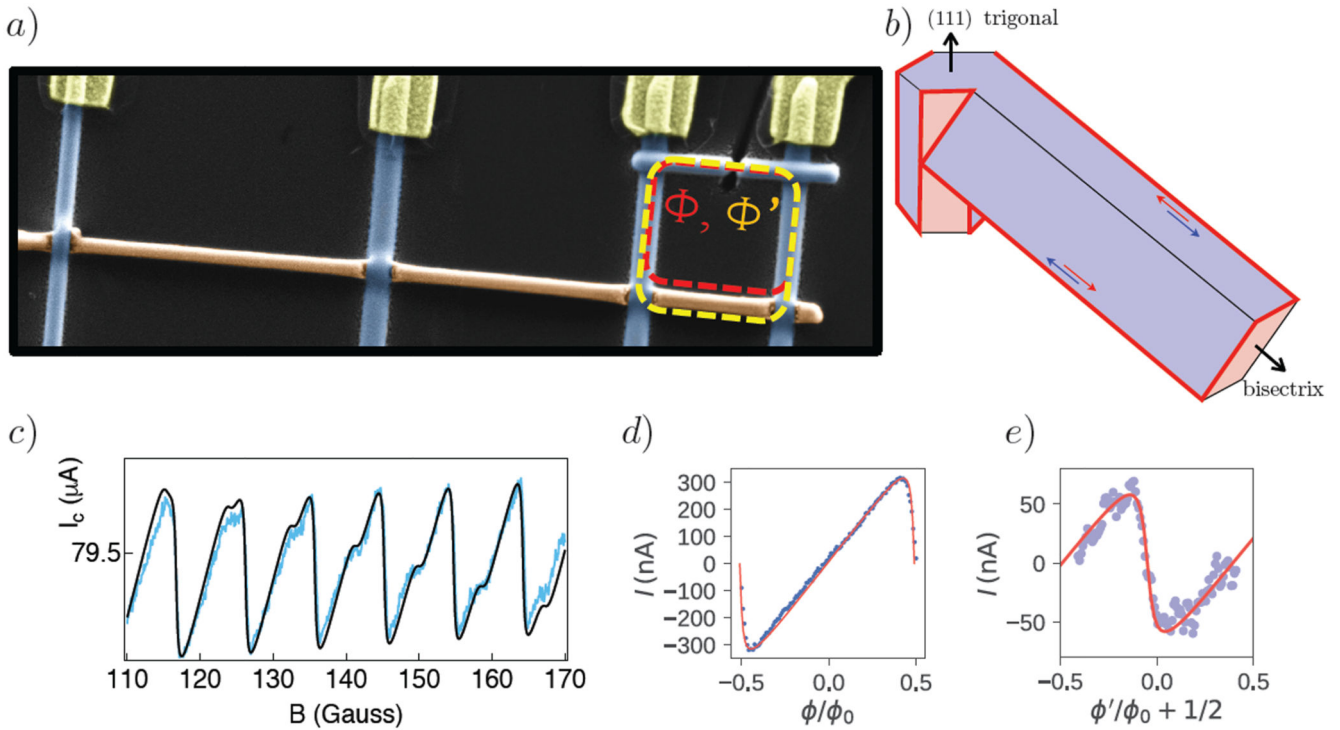
Fig. 3. Evidence for hinge states from Josephson-interference experiments.
a) Single-crystal bismuth nanowire (colored in brown) connected to superconducting electrodes (colored in blue). The wire has a parallelogrammatic cross-section. Its orientation along one of the bisectrix axes of bismuth was determined by electron diffraction, showing evidence of (111) facets parallel to the substrate. The 1.4 μm long, rightmost section of the wire, in parallel with a super-conducting weak link, forms an asymmetric SQUID. b) Schematic representation of the investigated bismuth nanowire of parallelogrammatic cross-section described above, indicating (red lines) the position of the experimentally identified topological hinge states in relation to the hinge states determined theoretically in a bismuth sample of hexagonal symmetry oriented along the trigonal [111] axis. c) The magnetic field dependence of the critical current shown is modulated by the current phase relation of the bismuth Josephson junction (whose critical current is much lower than the superconducting weak link). This current phase relation can be decomposed into the sum of two sawtooth waves d) and e) of different periods corresponding respectively to the internal and external area of the SQUID Φ and Φ' shown in a).